Editors' Suggestion

Topological phonons and thermoelectricity in triple-point metals

Sobhit Singh,[1,*] QuanSheng Wu,[2,3] Changming Yue,[4] Aldo H. Romero,[1] and Alexey A. Soluyanov[5,6,†]

[1]*Department of Physics and Astronomy, West Virginia University, Morgantown, West Virginia 26505-6315, USA*

[2]*Institute of Theoretical Physics, Ecole Polytechnique Fédérale de Lausanne (EPFL), CH-1015 Lausanne, Switzerland*

[3]*Theoretical Physics and Station Q Zurich, ETH Zurich, CH-8093 Zurich, Switzerland*

[4]*Beijing National Laboratory for Condensed Matter Physics, and Institute of Physics, Chinese Academy of Sciences, Beijing 100190, China*

[5]*Physik-Institut, Universität Zürich, Winterthurerstrasse 190, CH-8057 Zurich, Switzerland*

[6]*Department of Physics, St. Petersburg State University, St. Petersburg, 199034, Russia*

(Received 21 June 2018; published 15 November 2018)

Recently published discoveries of acoustic- and optical-mode inversion in the phonon spectrum of certain metals became the first realistic example of noninteracting topological bosonic excitations in existing materials. However, the observable physical and technological use of such topological phonon phases remained unclear. In this paper, we provide strong theoretical and numerical evidence that for a class of metallic compounds (known as triple-point topological metals), the points in the phonon spectrum, at which three (two optical and one acoustic) phonon modes (bands) cross, represent a well-defined topological material phase, in which the hosting metals have very strong thermoelectric response. The triple-point *bosonic* collective excitations appearing due to these topological phonon band-crossing points significantly suppress the lattice thermal conductivity, making such metals *phonon glass*like. At the same time, the topological triple-point and Weyl *fermionic* quasiparticle excitations present in these metals yield good electrical transport (*electron crystal*) and cause a local enhancement in the electronic density of states near the Fermi level, which considerably improves the thermopower. This combination of *phonon glass* and *electron crystal* is the key for high thermoelectric performance in metals. We call these materials topological thermoelectric metals and propose several compounds for this phase (TaSb and TaBi). We hope that this work will lead researchers in physics and materials science to the detailed study of topological phonon phases in electronic materials, and the possibility of these phases to introduce more efficient use of thermoelectric materials in many everyday technological applications.

DOI: 10.1103/PhysRevMaterials.2.114204

I. INTRODUCTION

By now, an almost complete classification of possible topological *fermionic* excitations in noninteracting systems has been constructed [1,2] and material examples hosting many of these classified phases are ubiquitous. This classification includes the so-called triple-point metals [3–7], in which a symmetry-protected crossing of three bands occurs close to the Fermi level, resulting in topological fermionic excitations. Here we claim that electronic crystalline compounds also have topologically protected *bosonic* excitations that result in nonstandard thermoelectric properties of the hosting materials.

Topological bosonic modes were proposed and realized in classical mechanical systems [8–10], where oscillations of pendulums are purely classical, but realize the same physics, as some quantum electronic systems do [11,12]. Another realization of topological bosonic states came from experiments on photonic crystals [13–20], providing a realization of Dirac, Weyl, and nodal line phases of bosons in a *bosonic* system. Several very recent works described the realization of topological bosonic modes in *electronic* systems [21–23]. For example, the appearance of a bosonic triple-point analog of a triple-point fermion in the phonon spectrum of several existing compounds is discussed in Ref. [22]. Phononic Weyl points were also reported in these metallic materials. Nonetheless, unlike the observable effects of topological fermionic excitations, no observable physical effect of these topological bosonic excitations was predicted.

The topological character of bosonic (phononic) Weyl points can be easily proven following the direct analogy with fermionic Weyl points. In fact, not only the methodology of computing chiralities of electronic Weyl points can be used for their phonon analogues, but even the same, already developed software for fermionic topological excitations [24,25] reveals the topology in this case. However, the topological origin of the triple point in the phonon spectrum is more complicated to capture.

Here we provide the proof of the topological nature of a triple-point phonon. We *add several metals* to the compounds described in Ref. [22]. Most importantly, we provide the topology-mediated observable physical effect, proving that the presence of triple-point phonons makes these topological metals the most efficient thermoelectric metals of those known to date. We show in detail that the enhanced thermoelectric response is driven by the topological band crossings present in the phonon spectrum.

In this work, we investigated the electronic and vibrational properties of nine compounds from TaX and NbX

*smsingh@mix.wvu.edu

†soluyanov@itp.phys.ethz.ch

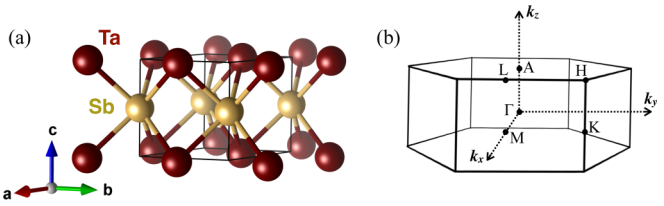

FIG. 1. (a) Crystal structure of TaSb compound in WC-type $P\bar{6}m2$ space group. Ta atoms (maroon) occupy the (2/3, 0.0, 2/3) site, and Sb atoms (golden) occupy the (0.0, 1/2, 0.0) site. The unit cell contains one Ta and one Sb atom. (b) Brillouin zone (BZ) of TaSb.

(X = N, P, As, Sb, Bi) families, considering all of them to have the tungsten carbide (WC)-type crystal structure (space group 187). The lattice parameters, electronic band structures, and phonon band structures of all these compounds are given in the Supplemental Material (SM) [26]. Our calculations reveal that TaP, TaAs, TaSb, TaBi, NbP, NbSb, and NbBi compounds exhibit triple-point and Weyl *fermionic* excitations, whereas, TaN and NbN compounds only have triple points in their electronic spectrum, as shown in the SM [26].

The *phonon* structure of all these compounds is similar, except for TaSb and TaBi compounds, in which an optical and acoustic phonon mode inversion takes place in the phonon spectrum. In the electronic spectrum, a similar band inversion between occupied and unoccupied states is a signature of the nontrivial topology. The same is true for crossings of optical and acoustic phonon modes, as we prove below. We will show that the presence of such topologically protected phonon mode crossings (i.e., triple-point phonons) significantly suppresses the lattice thermal conductivity, and thereby enhances the thermoelectric performance of these special topological metals.

In the following, we choose the compound TaSb as a prototype for the detailed illustration of topological features in the electronic and vibrational properties. The lowest energy crystal structure of TaSb is shown in Fig. 1. Our calculations indicate that this structure is stable at 0 K and at room temperature (see SM [26]). This paper is organized as follows: After the Introduction, we demonstrate the topological nature of electronic properties in Sec. II, and then we discuss the topological nature of phonons in Sec. III. Section IV deals with the thermoelectric response of triple-point metals, which is followed by a Summary section. All the theoretical derivations together with numerical details are presented in the Appendix.

II. ELECTRONIC BAND STRUCTURE OF TaSb

The electronic band structure of TaSb, calculated along the high symmetry directions of the Brillouin zone (BZ) with spin-orbit coupling (SOC), is shown in Fig. 2(d). Figures 2(a)–2(b) represent the Sb and Ta orbitals projected fat bands calculated in absence of SOC. Figure 2(a) indicates that Sb–5p_y and Sb–5p_z orbitals compose only the valence band states near the Fermi level, whereas the Ta-3d orbitals predominantly contribute to both the conduction and the valence bands [see Fig. 2(b)]. One can notice the presence of two evenly dispersed gapless points near the Fermi level, marked by magenta circles in Fig. 2(a), along the $M-K$ and $K-\Gamma$ directions. A further analysis of the electronic band structure near K-point reveals that these gapless points belong to a Dirac nodal line centered at the K-point. This Dirac nodal line primarily appears due to the inverted band ordering of Ta–$d_{x^2-y^2}$ and Ta–d_{yz+zx} orbitals near K-point [see Fig. 2(b)]. Additionally, the inverted band ordering of multiple Ta–d orbitals along the $\Gamma-A$ direction yields another fourfold degenerate gapless nodal line (marked by a magenta rectangle). This nodal line is protected by the C_{3v} rotational symmetry of the crystal and it is composed of Ta–d_{z^2}, $d_{x^2-y^2}$, d_{zx}, d_{xy} orbitals.

In the presence of SOC, the spin degeneracy of electronic bands is lost except at the time-reversal-invariant-momenta (TRIM) points. The Dirac nodal line surrounding the K-point disappears and an energy gap opens along the $M-K-\Gamma$ path [Fig. 2(d)]. The SOC-induced energy gap is about ~ 0.18 eV at this point, due to the large SOC of Ta and Sb atoms. A careful analysis of the bands away from the high-symmetry direction manifests that the gapless Dirac nodal line breaks into pairs of gapless Weyl points located at the same energy near the K-point. These pairs of Weyl points share opposite topological charge and they feature a source and a sink of Berry curvature in momentum space. These Weyl points are of type-I character and they have already been discovered in experiments [27–29]. Although SOC breaks the Dirac nodal line into type-I Weyl points, it does not destroy the gapless nodal line along $\Gamma-A$ completely. However, SOC partially lifts the degeneracy of the gapless nodal line from fourfold to twofold. It is noteworthy that the gapless nodal line lies exactly at the Fermi level. Two triply degenerate gapless nodal points (TP1 and TP2) appear at the ends of the nodal line as depicted in Fig. 2(d). These gapless points, known as triple points, emerge at the touching point of three bands (two valence and one conduction band) near the Fermi level as shown in the inset of Fig. 2(d) and are protected by the C_{3v} rotational symmetry and vertical mirror symmetries of the crystal [3]. The exact location of the triple points along $\Gamma-A$ path are: TP1 (0, 0, 0.298 $\frac{2\pi}{c}$) and TP2 (0, 0, 0.398 $\frac{2\pi}{c}$).

The existence of three-component fermions has been recently confirmed by angle-resolved photoemission spectroscopic (ARPES) measurements on MoP crystals [7]. The work of Ref. [3] predicted the existence of two topologically distinct types of triple-point metals (type A and type B). These two types can be easily classified by looking at the crystal symmetry of a system and the total number of accompanying nodal lines. The conditions for the appearance of the two types of triple-point fermions, the topological differences between them, and a list of hosting space groups are given in detail in Ref. [3]. All the TaX and NbX (X = P, N, As) family compounds having $P\bar{6}m2$ space group host topologically protected type-A triple-point fermions, connected by a single nodal line (see SM [26]).

Although there is no clear signature of Weyl points near the gapless nodal line and the triple points in Fig. 2(d), previous works reported the presence of type-II Weyl points near such gapless nodal lines [3,4]. Therefore, to pin down the location and chirality of all Weyl points, we perform a comprehensive analysis of the electronic structure near the Fermi level. We

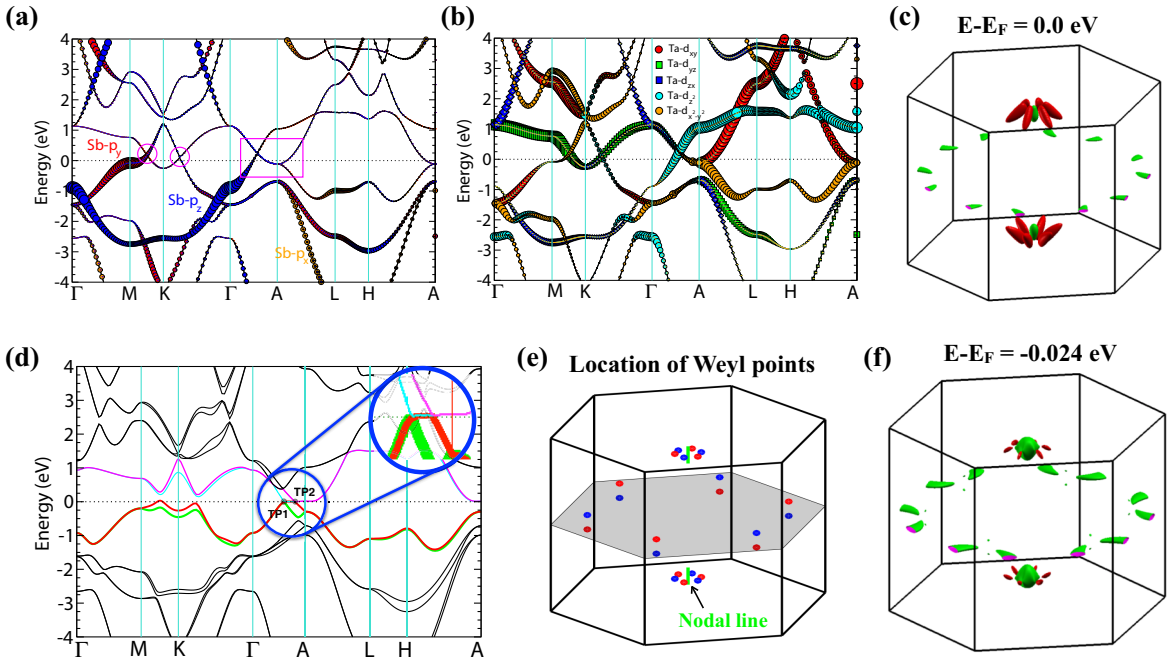

FIG. 2. (a) and (b) represent the electronic band structure calculated without inclusion of SOC. Projection of the Sb-p atomic orbitals is shown in panel (a) while projection of Ta-d orbitals is shown in panel (b). The magenta circles mark the location of points that belong to a Dirac nodal line centered at K-point, and magenta rectangle depicts the location of gapless nodal line present along the $\Gamma - A$ path. Panel (d) represents the electronic band structure calculated with SOC. The inset of panel (d) shows the enlarged view of the gapless nodal line. The locations of triple points (TP1 and TP2) at the end of the gapless nodal line are marked by black circles. For better visibility, bands near the Fermi level are plotted in different colors. Location of all the Weyl points present in the Brillouin zone are shown in panel (e). (For their exact locations, see Table I). Red (blue) spheres denote the Weyl points having positive (negative) chirality. The green lines mark the location of the gapless nodal line. Six pairs of Weyl points that appear in the shaded $k_x - k_y$ plane are of type I, while the other six pairs of Weyl points that surround the gapless nodal line are of type II. Panels (c) and (f) show the Fermi surface calculated at $E - E_F = 0.0$ eV and $E - E_F = -0.024$ eV, respectively. One can observe the formation of type-II Weyl points as touching points of electron and hole pockets along the $\Gamma - A$ path.

evaluate the energy gap (ΔE) between the Nth and $(N+1)$th bands in the 3D BZ; i.e., $\Delta E = E(N+1) - E(N)$. Here, N is the total number of occupied bands. Such obtained gapless points mark the location of Weyl points, and the obtained gapless line is a representative of the nodal line in BZ. We further integrate the Berry curvature in a small sphere enclosing each individual Weyl point, and thus we calculate the topological charge of each Weyl point [24,25]. Figure 2(e) shows the location and topological charge of all Weyl points. We observe that six pairs of type-I Weyl points appear near $k_z = 0$ plane at $E - E_F = -7$ meV energy. The exact location of a pair of Weyl points close to the K-point is (according to the tight-binding calculations): $(0.486\frac{2\pi}{a}, -0.243\frac{2\pi}{b}, \pm 0.0421\frac{2\pi}{c})$. We also observe two gapless nodal lines (marked by green color)

TABLE I. Coordinates of Weyl points and triple points (TP) present in TaSb.

	Coordinates
Triple-points (TP)	TP1 $\left(0.0,\ 0.0,\ \pm 0.298\frac{2\pi}{c}\right)$
	TP2 $\left(0.0,\ 0.0,\ \pm 0.398\frac{2\pi}{c}\right)$
Weyl-points (type I) near K	$\left(0.486\frac{2\pi}{a}, -0.243\frac{2\pi}{b}, \pm 0.0421\frac{2\pi}{c}\right)$
Weyl-points (type II) near TP	$\left(\pm 0.034\frac{2\pi}{a}, \pm 0.034\frac{2\pi}{b}, \pm 0.357\frac{2\pi}{c}\right)$
	$\left(\pm 0.06\frac{2\pi}{a},\ 0.00, \pm 0.357\frac{2\pi}{c}\right)$

connecting the triple points TP1 and TP2 in the full BZ. Surprisingly, we discover three additional pairs of Weyl points located near each gapless nodal line. These Weyl points appear at $k_z = \pm 0.357\,(\frac{2\pi}{c})$ near $E - E_F = -24$ meV energy. The energy band dispersion near these Weyl points suggests that these Weyl points have type-II character [30]. The type-II Weyl fermions appear at the touching points of the electron and hole pockets in reciprocal space, which happens due to the tilted linear dispersion of spin nondegenerate bands near Fermi level.

We illustrate the evolution of the Fermi surface calculated at different energy values in Figs. 2(c) and 2(f). One can evidently observe the formation of both type-I and type-II Weyl points in the Fermi-surface plots. The touching of electron and hole pockets forming six isolated type-II Weyl points can be noticed in Fig. 2(f).

The presence of Weyl points in the bulk suggests the existence of ARPES-observable open Fermi arcs at the surface of Weyl semimetals [31]. Therefore, we study the topological features of surface states by means of the tight-binding model constructed using the maximally localized Wannier functions method [32,33], using WannierTools software [25]. The results for different terminations of (100) and (001) surfaces are presented in the SM [26]. The positive and the negative Weyl points project themselves onto each other on the (001) surface,

thus making the Fermi arc invisible on the (001) surface of BZ. However, we do observe open Fermi arcs connecting opposite Weyl points on the (100) surface, where the projected Weyl points do not neutralize their nontrivial features (see SM [26]). Since the Weyl points are well dispersed on the (100) surface, the connecting Fermi arcs are quite long in momentum space which makes them accessible in ARPES measurements.

III. TOPOLOGICAL PHONONS IN TaSb

All the considered compounds have two atoms per primitive unit cell, hence having six phonon bands (three acoustic and three optical) in the spectrum. It is shown in Appendix A that a phonon triple point appears in those compounds, where the masses of atoms forming the material satisfy the following condition for phonon mode inversion: The frequency gap Δ between the acoustic and optical phonon bands at the A-point of BZ has to become negative for these bands to invert:

$$\Delta \propto \sqrt{\beta_{\parallel}} - \sqrt{\beta_{\perp}\frac{m}{M}}. \tag{1}$$

Here, $\beta_{\parallel}$ and $\beta_{\perp}$ are the in-plane and out-of-plane second-order interatomic force constants between the atoms of masses m and M ($m < M$), respectively.

This relationship is verified by our calculations: Δ decreases systematically with the increase of m/M ratio. For TaN ($m/M = 0.0774$), TaP ($m/M = 0.1711$), and TaAs ($m/M = 0.414$) compounds, the obtained Δ values are 200.5, 115.1, and 14.4 cm^{-1}, respectively, but for TaSb ($m/M = 0.6731$) and TaBi ($m/M = 0.8658$) compounds Δ become negative (-16.7 and -27.8 cm^{-1}, correspondingly) indicating the inversion of phonon modes in the BZ. In addition to increasing m/M ratio, $\beta_{\perp} > \beta_{\parallel}$ condition is essential to observe the phonon mode-inversion in the BZ. Results of Li *et al.* [22] further corroborate the aforementioned relationship (see Appendix A).

We thus conclude that while the electronic properties of TaSb in $P\bar{6}m2$ group are similar to those of other triple-point metals of TaX and NbX family (X = N, P, As), the phonon spectrum of TaSb and TaBi compounds makes them distinct from the other triple-point metals in the considered material set. In particular, we observe that one acoustic band (No.. 3) and two degenerate optical bands (No. 4 and No. 5) in TaSb and TaBi compounds intersect each other along the Γ-A path forming two triply degenerate phonon points (TDP) as shown in Fig. 3(a) for TaSb. The atomic vibrations corresponding to these phonon bands are illustrated in Figs. 3(b)–3(d). The TDPs are located at frequency $\approx$145 cm^{-1} and at $\mathbf{q} = (0, 0, \pm 0.428)$. The phonon mode inversion can be noticed above the TDP (along k_z), where two degenerate optical phonon bands (No. iv and No. v) unusually appear at lower frequencies than the acoustic phonon band (No. iii). The phonon mode inversion, at the high-symmetry point A(0, 0, $\pm\frac{\pi}{c}$), is indicative of the nontrivial topological nature of the vibrational properties in TaSb compound. Despite the isoelectronic similarity of all the considered compounds, such phonon band-inversion along Γ-A path present only in TaSb and TaBi, is due to the fact that atoms of relatively similar masses constitute these compounds.

Topological classification of noninteracting fermionic excitations is built from the symmetry analysis of tight-binding models. Analogously, topological classification of phonons (bosonic excitations) can be built from the analysis of dynamical matrices (a good, although not fully complete in terms of various symmetry constraints, exposition of this approach is presented for mechanical vibrations in Ref. [9]).

Starting from this point of view, let us now prove that the TDP indeed has a topological origin, for which a topological invariant can be defined (see Appendix B for more details). To capture the presence of fermionic triple points in the band structure, two triple points are enclosed into a surface in the BZ. Computation of the Wilson loop of lower-lying bands on this surface gives a robust topological signature of triple fermionic points in metals [3]. Although TDPs also appear in pairs in the BZ, unlike the case of Weyl points, a direct analogy to the fermionic approach to obtain the topological invariant does not work for TDPs.

However, we can still find the path to define a topological invariant if we keep in mind that type-A triple points in electronic band structure are connected by a single nodal line, which is topologically trivial, having the 0 value of the Berry phase (ϕ_B) of occupied bands on any circular path enclosing it. Nonetheless, the hidden topology is revealed by applying the Zeeman field [3], which splits the two triple points into four Weyl points.

We apply a similar trick here to capture the topology of TDPs. Instead of the Hamiltonian in the electronic case, we deal with the dynamical matrix, the eigenvalues of which, similar to the type-A triple point electronic Hamiltonian case, connect the two TDPs by a degenerate line (this line in Fig. 3(a) is formed by the degenerate phonon bands iv and v). The degeneracy between phonon bands 4 and 5, as well as between bands iv and v, occurs due to the presence of C_{3v} symmetry in the considered crystal lattice, because the xx and yy force constants transform like x and y coordinates. The latter transform in the same way as p_x and p_y orbitals that in the C_{3v} group form a two-dimensional irreducible representation E, thus enforcing the degeneracy seen in Fig. 4(a). The degeneracy line (not a loop, but an open line) in the BZ of bands iv and v is illustrated in Fig. 4(d).

Analogously to the nodal line in type-A electronic triple points, this line of degenerate modes iv and v [on the right side of the crossing point in Fig. 3(a)] carries 0 Berry phase (ϕ_B) computed for the lower-lying phonon bands around the path S^1 of Fig. 4(d). To reveal the topology of the TDP, we use the trick similar to Zeeman splitting mentioned above. To do that, we modify the entries in the dynamical matrix in a way that corresponds to changing the semiclassically understood "spring constants" connecting atoms along the x and in the y directions (that can be related to the corresponding interatomic bond strength). This modification splits the degeneracy of the phonon nodal line, as illustrated in Figs. 4(b) and 4(c).

It turns out that such a splitting gaps the phonon bands 4(iv) and 5(v) along the (Γ-A) direction of the BZ. However, away from this line we still see the nodal *loops* formed by the inverted bands iv and v. Computation of ϕ_B of the lower-lying phonon bands along the path S^2 linked with this degeneracy loop gives $\phi_B = \pi$, thus proving the topological nature of the

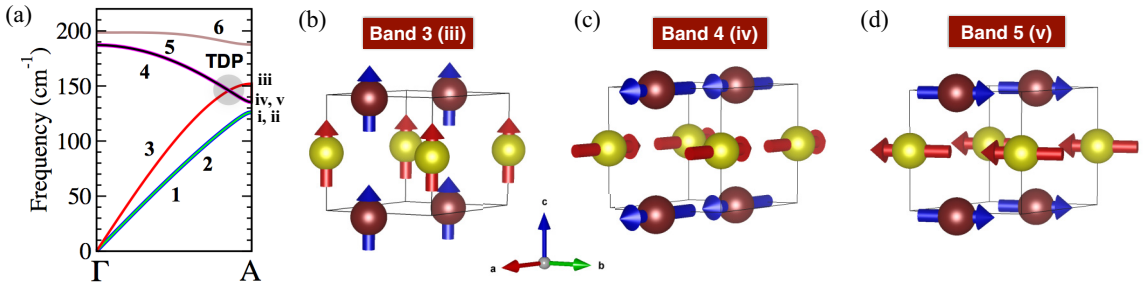

FIG. 3. (a) Part of the phonon spectrum of TaSb. The triply degenerate point (TDP), at which phonon bands 3(iii), 4(iv), and 5(v) meet is the topologically protected triple point of phonons (another such point is located in the other direction in the BZ on the same C_{3v}-symmetric line). Panels (b)–(d) explicitly illustrate the atomic vibrations corresponding to the overlapping phonon modes 3(iii), 4(iv), and 5(v), correspondingly. The enumeration of phonon bands is made with numbers (1..6) and (i..vi) "before" and "after" the crossing point, to stress the change in phonon band ordering by using different number styles for ordinary and inverted phonon band orderings.

TDPs, just like the splitting of electronic triple points into four Weyl points by the Zeeman field proves the topological origin of type-A fermionic triple-points.

Despite this proof of the topological origin of TDPs, the more important question is the observable physical consequences, associated with these topological phonon modes. Although our calculations of the surface phonon spectrum of TaSb reveal topological surface modes, they are not really observable, being heavily intermixed with the bulk modes (see SM [26]). The work of Ref. [22] demonstrated evidence of similar nontrivial surface modes (open Fermi arcs) in TiS and HfTe compounds that also host TDPs in their phonon spectra. However, similar to the case of TaSb, the phonon surface modes in these compounds are also buried in the projection of bulk phonon modes. For this reason, we explore another possible signature of nontrivial topological excitations, that is, transport properties. Of these properties, the one closely related to phonons (although with a large contribution from electrons as well), is the thermal transport [34]. For this reason, we study the effect of the phonon TDPs on the thermoelectric properties of hosting metals, and find them to be among the most efficient metallic thermoelectrics.

IV. ENHANCED THERMOELECTRIC RESPONSE

The performance of thermoelectric materials at temperature T is usually determined by the figure of merit,

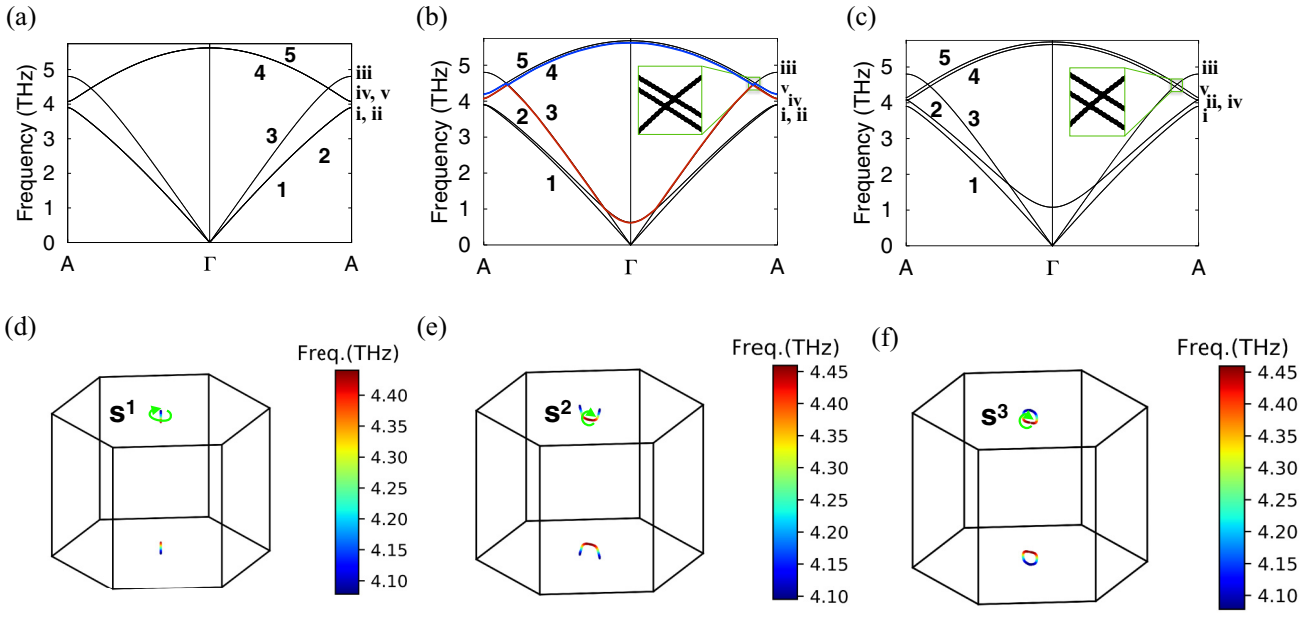

FIG. 4. (a) The phonon spectrum of TaSb along the C_{3v}-symmetric line of the BZ. Doubly degenerate phonon bands (4,5) and (iv,v) can be seen. (b) The phonon spectrum of TaSb with the xx and yy force constants in the dynamical matrix made unequal for Ta. The degeneracy of (4,5) and (iv, v) is lifted. (c) The phonon spectrum of TaSb with the xx and yy force constants in the dynamical matrix made unequal for Sb. The degeneracy of (4,5) and (iv, v) is lifted. (d) The nontopological *open nodal line* formed in the BZ by bands iv and v of panel (a). The loop S^1 encircles this line, but $\phi_B(S^1) = 0$. (e) The *closed nodal loop* formed by bands iv and v in the BZ for the case of panel (b) away from the Γ-A line. The contour S^2 links with this loop and $\phi_B(S^2) = \pi$. (f) The *closed nodal loop* formed by bands iv and v in the BZ for the case of panel (c). For a contour S^3 linked with this loop, $\phi_B(S^3) = \pi$.

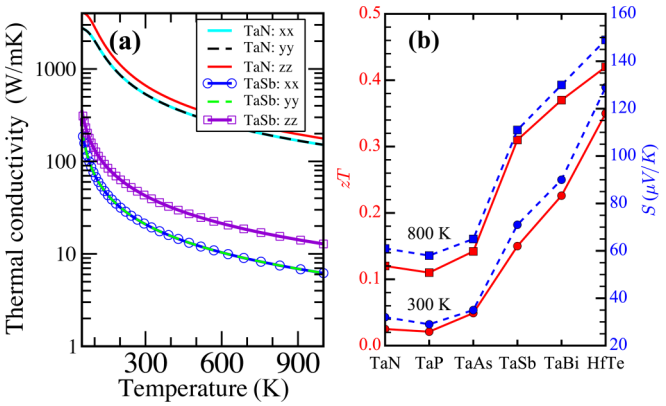

FIG. 5. (a) Variation of different components of lattice thermal conductivity tensor (κ_{ph}) against temperature T for TaN and TaSb along x, y, and z directions of crystal. (b) Comparison of maximum zT (red) and Seebeck coefficients (blue) obtained for electron doping at 300 K (circles) and 800 K (squares).

$zT = \frac{S^2\sigma}{\kappa_{el}+\kappa_{ph}}T$, where quantities S and σ are Seebeck coefficient and electrical conductivity, whereas, κ_{el} and κ_{ph} are the electronic and phononic (lattice) contributions to the thermal conductivity of material. A combination of large S and large σ together with a small κ ($=\kappa_{el}+\kappa_{ph}$) is required to achieve large zT. In other words, a good thermoelectric is a good conductor of charge carriers (i.e., electron-crystal) and a bad conductor of phonons (i.e., phonon-glass). Thus, in case of metals hosting coexisting topological electron and phonon excitations, we expect a significant benefit toward the enhancement of zT.

First, the presence of topologically protected phonon band crossings considerably suppresses the lattice thermal conductivity due to the increased phonon scattering centers (see SM [26] for more details). The κ_{ph} (and the phonon mean free path) in TaSb is almost two orders in magnitude smaller compared to that of in TaN, which is a metal without TDPs (Fig. 5 and more details in the SM [26]). According to the Wiedemann-Franz law, $\kappa_{el} = L_0 T\sigma$, where L_0 is the Lorenz number and τ is the electron-phonon relaxation time [35]. Since $\sigma/\tau \sim 10^{20}$ $1/\Omega$ ms at low-doping concentrations for all the studied metals, the κ_{el} (which mainly governs κ at high T) is also in the same order of magnitude for all TaX compounds. Therefore, reduction in κ_{ph} (which dominates κ at low T) causes a net decrease in κ of TaSb and TaBi (see SM [26]).

Second, there is an increase in the Seebeck coefficient (S) of TaSb and TaBi. In particular, we notice a local enhancement in the electronic density of states (DOS) near the Fermi level as we go from TaN to TaBi. This occurs due to the flattening of electronic bands at the Fermi level in TaSb and TaBi compounds (see SM [26]). According to the Mahan-Sofo theory [36], such a situation yields an increase in S, which in turn improves zT. In general, the sharper is the local increase in DOS at the Fermi level, the larger is the enhancement in S. Decrease in κ_{ph} and an increase in S combine to improve the overall thermoelectric efficiency zT.

In Fig. 5, we compare the zT of all the TaX family compounds considered in this work, as well as one of the previously predicted TDP compounds HfTe [22]. Comparison of other thermoelectric quantities is presented in Appendix C. Although the illustrated zT of these compounds is smaller than that of the best-known narrow band gap semiconductor thermoelectrics (having $zT \approx 1$), it is among the best known *thermoelectric metals* and performs much better compared to nontopological metals, for which zT ranges from $0.0001-0.001$ [37–39]. Notably, we find that HfTe, a triple-point metal hosting TDPs predicted in Ref. [22], exhibits considerably large zT (maximum $zT = 0.35$ at 300 K and 0.42 at 800 K for electron doping case) compared to that of TaSb and TaBi compounds due to its relatively large Seebeck coefficient (maximum $S = 129\ \mu$V/K at 300 K and $149\ \mu$V/K at 800 K for electron doping). The results that we obtain here for TaSb, TaBi, and HfTe triple-point metals put these materials in the list of the best thermoelectric metals known to date, along with a lower symmetry (space group #109) TaAs [40] and recently reported HgTe [41].

V. SUMMARY

In summary, our work provides an illustration of the use of topological phases of phonons in existing electronic compounds and materials TaSb and TaBi, which combine electronic and bosonic (phononic) topological phases. The associated topological excitations—fermions and phonons—give rise to enhanced thermopower and thermoelectric response in considered metals. The topological phonon modes considerably suppress the lattice thermal conductivity without disrupting the electronic transport in the bulk crystal, whereas the topological electronic bands near the Fermi level give rise to a local increase in the DOS at the Fermi level causing an increment in the thermopower. Having illustrated the approach to prove the topological phase of phonon spectrum and the role of nontrivial phonon modes on the thermal transport properties, we hope this work will motivate further studies of the effects of topologically nontrivial phonons on the material properties, including thin films and metal/semiconductor heterostructures, where the effects of topology and phonon scattering can be more pronounced. Since the topological nontriviality of bulk phonon modes guarantees the existence of gapless phonon surface states, which highly overlap with the bulk phonons (in the studied materials) providing more phonon scattering channels and causing further reduction of the lattice thermal conductivity in 2D, it would be interesting to investigate the properties of the topological thermoelectric metals in 2D as well as in specially designed metal/semiconductor heterostructures.

ACKNOWLEDGMENTS

This work used the Extreme Science and Engineering Discovery Environment (XSEDE), which is supported by NSF Grant No. OCI-1053575. Additionally, we acknowledge support from Texas Advances Computer Center (TACC), Bridges supercomputer at Pittsburgh Supercomputer Center and Super Computing Systems (Spruce and Mountaineer) at West Virginia University. A.H.R. and S.S. acknowledge support from National Science Foundation (NSF) DMREF-NSF 1434897, OAC-1740111,

and DOE DE-SC0016176 projects. S.S. acknowledges support from the Dr. Mohindar S. Seehra Research Award and the Robert T. Bruhn Research Award at West Virginia University. Q.S.W and A.A.S. acknowledges the support of Microsoft Research NCCR QSIT and NCCR MARVEL grants. We sincerely thank Olle Hellman for fruitful discussions.

APPENDIX A: PHONONS BAND-INVERSION IN TaSb

We observe that one acoustic branch (No. 3) and two degenerate optical branches (No. 4 and No. 5) intersect each other along the $\Gamma - A$ path, forming a gapless triple-degenerate-point (TDP) as marked in Fig. 3(a). To rule out the possibility of artifacts in the plotting, we analyze the polarization of each phonon eigenvector along the $\Gamma - A$ path calculated using a very dense q mesh. Our results remarkably confirm that the phonon band crossing at TDP is real. The TDP is located at frequency 145 cm^{-1} and at (0, 0, 0.428) q point. It is worth mentioning that this phonon band inversion along $\Gamma - A$ path is missing for the case of other triple-point metals (except TaBi), even though all triple-point metals share isoelectronic properties. One main reason of the existence of phonon band inversion is the fact that the atoms of almost equal masses constitute the TaSb and TaBi compounds. When there is a significant difference in the mass of the constituent atoms, the above-mentioned phonon band crossing does not take place and a wide frequency gap appears in the phonon spectrum.

The nature of the atomic vibrations corresponding to each phonon eigenmode near the TDP is shown in Figs. 3(b)–3(d). The third phonon band corresponds to the acoustic (in-phase) vibration of Ta and Sb atoms oscillating in a plane perpendicular to the $x - y$ plane of cell. On the other hand, the fourth and fifth phonon bands represent the optical vibrations (out-of-phase) of Ta and Sb atoms in the $x - y$ plane of cell. These two optical phonon branches are degenerate along the $\Gamma - A$ path due to the crystal symmetry of TaSb compound. At a q point below the TDP, the acoustic mode (third band) has lower frequency than that of the optical modes (4 and 5). However, above the TDP, the acoustic mode unusually attains higher frequency compared to the frequency of the optical modes, thus leading to a band inversion in the phonon spectra along with formation of a triple-degenerate point along $\Gamma - A$ path. Also, the Ta atom oscillates with a larger amplitude in the inverted acoustic mode (third band). The TDP is protected by the C_{3v} rotational symmetry of the TaSb crystal. The excitations near the TDP yield three-component bosonic quasiparticles in the present system.

The competition of the in-plane and out-of-plane interatomic force constants between the atoms of comparable mass could be the primary reason of the phonon-band inversion in TaSb and TaBi compounds. Therefore, we study the vibrational modes of a diatomic system considering a harmonic approximation for the interatomic potential. Our analysis suggests that the frequency gap (Δ) between the optical (branch 4 or 5) and acoustic phonon branches (branch 3) at the BZ edge $(0, 0, \frac{\pi}{2})$ is

$$\Delta = \sqrt{\frac{2\beta_{\parallel}}{m}} - \sqrt{\frac{2\beta_{\perp}}{M}}, \tag{A1}$$

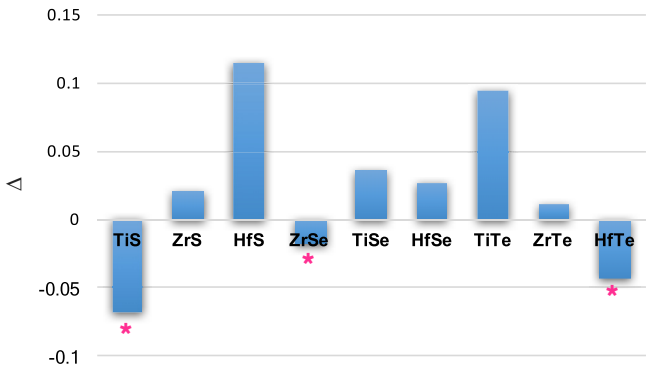

FIG. 6. Normalized phonon frequency gap (Δ) calculated near the A-point of BZ for the set of nine compounds reported in Ref. [22]. A negative value of Δ implies the presence of phonon band inversion. Only three compounds (marked with asterisk) show negative Δ.

i.e.,

$$\Delta \propto \sqrt{\beta_{\parallel}} - \sqrt{\beta_{\perp}\frac{m}{M}}. \tag{A2}$$

Here, $\beta_{\parallel}$ and $\beta_{\perp}$ are the in-plane and out-of-plane second-order interatomic force constants between the atoms of mass m and M ($m < M$), respectively. We observe that the frequency gap (Δ) decreases systematically with increase in the m/M ratio. In addition to increasing m/M ratio, $\beta_{\perp} > \beta_{\parallel}$ condition is essential to observe the phonon band inversion at the BZ edge.

To further test the validity of Eq. (A2) for phonon band inversion, we apply it on the data reported by Li *et al.* [22]. Figure 6 shows the calculated Δ $(=\sqrt{\beta_{\parallel}} - \sqrt{\beta_{\perp}\frac{m}{M}})$ for nine different compounds using the data from Ref. [22]. Here, we used normalized Δ by dividing it by the constant factors. Used atomic masses are given in the SM [26]. We notice that only three out of nine compounds can have negative Δ, and therefore only these three compounds (TiS, ZrSe, and HfTe) can host TDP in their phonon spectrum, which is consistent with the predictions in Ref. [22].

APPENDIX B: THEORETICAL DEMONSTRATION OF THE NONTRIVIAL TOPOLOGY OF PHONON MODES IN TaSb

Assuming $u^{\alpha}_{l,s}$ is the displacement of the sth atom in the lth unit cell along α ($\alpha = x, y, z$) direction, the total potential can be expanded according to u^{α}_{l} as

$$\Phi = \Phi_0 + \frac{1}{2}\sum_{l,s,\alpha}\sum_{l',s',\beta}\Phi^{l-l'}_{\alpha\beta,ss'}u^{\alpha}_{l,s}u^{\beta}_{l',s'} + \ldots \tag{B1}$$

where the first derivation is zero, due to the equilibrium state. The second derivation coefficient represents the force constant, which can be calculated in the first-principle calculations. There is a very important relation:

$$\sum_{l'}\Phi^{l-l'}_{\alpha\beta,ss'} = 0. \tag{B2}$$

So, $\Phi^{0}_{\alpha\beta,ss'} = -\sum_{l\neq 0}\Phi^{l}_{\alpha\beta,ss'}$

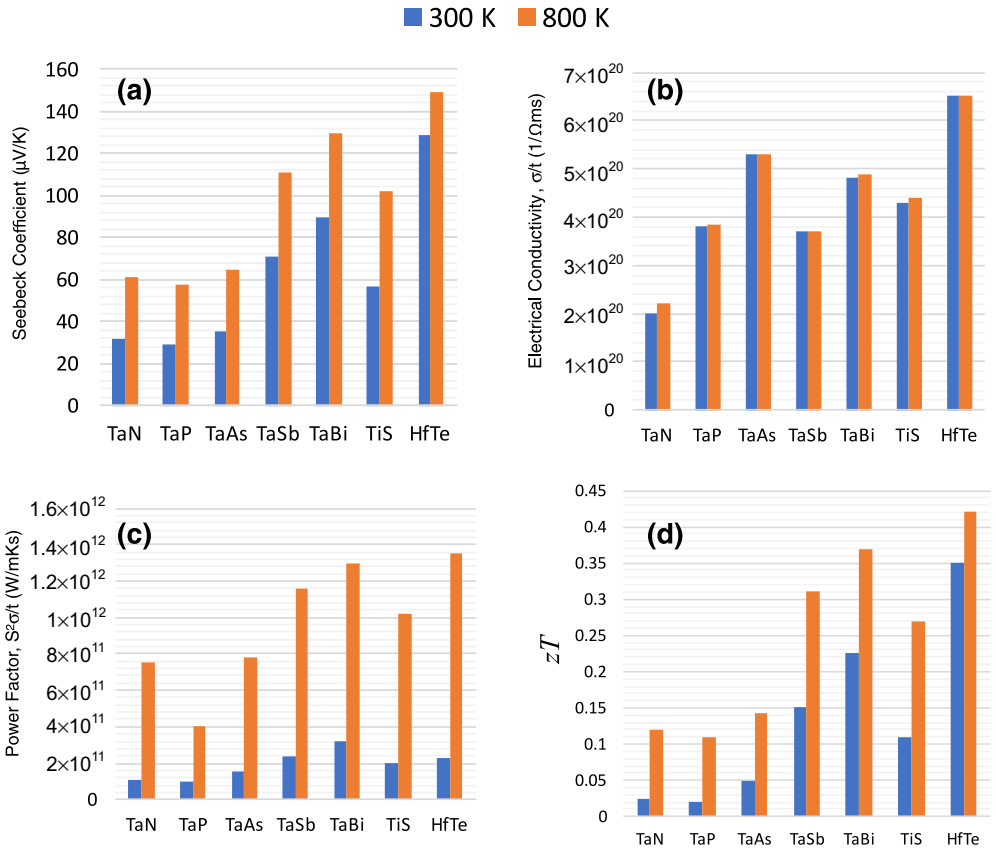

FIG. 7. (a) Maximum of Seebeck coefficient or thermopower, (b) maximum of electrical conductivity (σ/t) obtained at 300 K and 800 K, (c) maximum power factor at 300 K and 800 K, and (d) the theoretical maximum of zT. Above data is for the electron doping case.

In TaSb system, s = Ta, s' = Sb. Under the C_{3v} symmetry, $\Phi^0_{xx,ss}$ should be the same as $\Phi^0_{yy,ss}$, which leads to a trivial nodal line linking two triple points along $A-\Gamma-A$ shown in Figs. 4(a) and 4(d). A trivial nodal line means that the Berry phase along a close around the nodal line, like S^1 in Fig. 4(d), is zero. To study the topological structure of the nodal line in the spinless system, we studied two cases by manually modifying the lattice constant. One is that $\Phi^0_{xx,Ta-Ta} \neq \Phi^0_{yy,Ta-Ta}$, the other is $\Phi^0_{xx,Sb-Sb} \neq \Phi^0_{yy,Sb-Sb}$. The band structure and the nodal lines are shown in Fig. 4(a) and Figs. 4(d)–4(f), respectively. It is shown that the trivial nodal line would deform to a nontrivial nodal line with π Berry phase.

APPENDIX C: COMPARISON OF THERMOELECTRIC PROPERTIES

In Fig. 7 we compare the maxima of various thermoelectric properties of TaX obtained for electronic doping case. We also compare the thermoelectric properties of TaX with two other similar compounds predicted by Li *et al.*—HfTe and TiS [22]. We notice relatively smaller magnitude of thermoelectric effects for hole doping case (more details in the SM [26]).

APPENDIX D: NUMERICAL DETAILS

Density functional theory-based first-principles calculations were carried out using the projector augmented-wave (PAW) method as implemented in the VASP code [42,43]. We used the PBE exchange-correlation functional as parametrized by Perdew-Burke-Ernzerhof [44]. The SOC was employed by a second-variation method implemented in the VASP code. We considered five valence electrons of Ta ($5d^36s^2$) and five valence electrons of Sb ($5s^25p^3$) in the PAW pseudopotential. The lattice parameters were optimized until the Hellmann-Feynman residual forces were less than 10^{-4} eV/Å per atom. For convergence of the electronic self-consistent calculations, a total energy difference criterion was defined as 10^{-8} eV. We used 600 eV as kinetic energy cutoff of the plane-wave basis set and a Γ-type $10\times10\times10$ k-point mesh was employed to optimize the lattice parameters and the self-energy. The phonon calculations were performed for a $2\times2\times2$ supercell. The PHONOPY code [45] was used for the phonons post-processing. SOC was included in the phonon calculations. To verify the stability of the TaSb compound at room temperature, we performed room temperature molecular dynamics (MD) simulations for more than 9800 fs with a time step of 1 fs. The SOC was included in the MD simulations. In MD simulations, we employed a supercell of size $4\times4\times4$ to guarantee the decay of interatomic force constants within the supercell dimensions. The topological charge of the Weyl points and the surface state spectrum were calculated using the open-source WANNIERTOOLS code [25]. This code is based on the iterative Green's function mechanism and it performs the postprocessing of the Wannier tight-binding

model Hamiltonian obtained from the WANNIER90 [46]. We used Ta s, p, d, and Sb s, p orbitals as the initial projectors for construction of the Wannier tight-binding Hamiltonian. Details regarding the crystal structure and its stability are given in the SM [26].

1. Thermal conductivity and anharmonic high-temperature phonons

To accurately describe the high temperature anharmonicity of TaSb and TaN, we used *ab initio* molecular dynamics in combination with the temperature dependent effective potential technique (TDEP) [47–49] to extract effective interatomic force constants at finite temperature. The *ab initio* molecular dynamics simulations were carried out using the PAW method as implemented in VASP [42,43]. The simulation cell was constructed from a $4 \times 4 \times 4$ repetition of the unit cell (128 atoms). We used a set of seven volumes around equilibrium and ran molecular dynamics at 300 K using the Γ-point for BZ integration and an energy cutoff of 600 eV for about 10 000 time steps to ensure good coverage of the phase space. The temperature was controlled with a Nose-Hoover thermostat [50,51]. A 1.0 femtosecond time step was used in the MD calculations. From the forces obtained from uncorrelated configurations (one every 50 frames), folding into the unit cell is performed and the temperature dependent of the harmonic and anharmonic interatomic force constants are obtained. With this information, we obtain the lattice thermal conductivity.

For the other topological materials, we have used a slightly different approach. We have generated a series of 150 different uncorrelated configurations with a Gaussian distribution around a predefined temperature (lower than the Debye temperature). For each of those configurations, the forces are calculated from first principles and the same methodology described in the previous paragraph was followed. We find a very good convergence of results obtained from 150 uncorrelated configurations and that of obtained from the MD simulations described in the above paragraph.

2. Details of the thermoelectric properties calculations

We perform the calculation of the thermoelectric properties such as the thermopower or Seebeck coefficient (S), electrical conductivity (σ), the power factor ($S^2\sigma/\tau$), and the theoretical maximum figure of merit (zT). These thermoelectric properties were obtained using the solution of Boltzmann transport equations within the constant relaxation time approximation as implemented in the BoltzTrap code [52,53]. This theory allows us to calculate the Seebeck coefficient tensor independently of the electronic relaxation time (τ) while the electronic conductivity is dependent on τ. The code utilizes the rigid band approximation to change the carrier concentration by rigidly shifting the chemical potential (μ) into valence or conduction bands while the effects of temperature on the electronic bands are neglected. The carrier concentration was considered from range -1×10^{21} to 1×10^{21} cm^{-3}. The results obtained within the BoltzTrap code have shown very good agreement with experimental measurements, specially for bulk materials [54,55]. The lattice thermal conductivity evaluated from the TDEP code was used to estimate zT. The relaxation time (τ) obtained from the first-principles calculations (electron-phonon interaction) was found to vary in the order of 1 ps with increasing temperature. Therefore, we decided to choose $\tau = 1 \times 10^{-12}$ s. However, we observe negligible changes in zT with varying τ in ps range. This is as expected for systems with small κ_{ph} and relatively large κ_{el}.

[1] B. Bradlyn, J. Cano, Z. Wang, M. G. Vergniory, C. Felser, R. J. Cava, and B. A. Bernevig, Science **353**, aaf5037 (2016).
[2] B. Bradlyn, L. Elcoro, J. Cano, M. G. Vergniory, Z. Wang, C. Felser, M. I. Aroyo, and B. A. Bernevig, Nature **547**, 298 (2017).
[3] Z. Zhu, G. W. Winkler, Q. S. Wu, J. Li, and A. A. Soluyanov, Phys. Rev. X **6**, 031003 (2016).
[4] H. Weng, C. Fang, Z. Fang, and X. Dai, Phys. Rev. B **94**, 165201 (2016).
[5] G. W. Winkler, Q. S. Wu, M. Troyer, P. Krogstrup, and A. A. Soluyanov, Phys. Rev. Lett. **117**, 076403 (2016).
[6] S. Zaheer, S. M. Young, D. Cellucci, J. C. Y. Teo, C. L. Kane, E. J. Mele, and A. M. Rappe, Phys. Rev. B **87**, 045202 (2013).
[7] B. Q. Lv, Z. L. Feng, Q. N. Xu, X. Gao, J. Z. Ma, L. Y. Kong, P. Richard, Y. B. Huang, V. N. Strocov, C. Fang, H. M. Weng, Y. G. Shi, T. Qian, and H. Ding, Nature **546**, 627 (2017).
[8] R. Süsstrunk and S. D. Huber, Science **349**, 47 (2015).
[9] R. Süsstrunk and S. D. Huber, Proc. Natl. Acad. Sci. U.S.A. **113**, E4767 (2016).
[10] S. D. Huber, Nat. Phys. **12**, 621 (2016).
[11] C. L. Kane and T. C. Lubensky, Nat. Phys. **10**, 39 (2014).
[12] O. Stenull, C. L. Kane, and T. C. Lubensky, Phys. Rev. Lett. **117**, 068001 (2016).
[13] A. B. Khanikaev, S. Hossein Mousavi, W.-K. Tse, M. Kargarian, A. H. MacDonald, and G. Shvets, Nat. Mater. **12**, 233 (2013).
[14] L. Lu, J. D. Joannopoulos, and M. Soljacic, Nat. Photon. **8**, 821 (2014).
[15] K. Sun, W. V. Liu, A. Hemmerich, and S. Das Sarma, Nat. Phys. **8**, 67 (2012).
[16] J. Mei, Y. Wu, C. T. Chan, and Z.-Q. Zhang, Phys. Rev. B **86**, 035141 (2012).
[17] S. Raghu and F. D. M. Haldane, Phys. Rev. A **78**, 033834 (2008).
[18] L. Lu, L. Fu, J. D. Joannopoulos, and M. Soljacic, Nat. Photon. **7**, 294 (2013).
[19] M. C. Rechtsman, Y. Plotnik, J. M. Zeuner, D. Song, Z. Chen, A. Szameit, and M. Segev, Phys. Rev. Lett. **111**, 103901 (2013).
[20] W.-Y. He and C. T. Chan, Sci. Rep. **5**, 8186 (2015).
[21] T. Zhang, Z. Song, A. Alexandradinata, H. Weng, C. Fang, L. Lu, and Z. Fang, Phys. Rev. Lett. **120**, 016401 (2018).
[22] J. Li, Q. Xie, S. Ullah, R. Li, H. Ma, D. Li, Y. Li, and X.-Q. Chen, Phys. Rev. B **97**, 054305 (2018).
[23] M. Esmann, F. R. Lamberti, P. Senellart, I. Favero, O. Krebs, L. Lanco, C. Gomez Carbonell, A. Lemaître, and N. D. Lanzillotti-Kimura, Phys. Rev. B **97**, 155422 (2018).

[24] D. Gresch, G. Autès, O. V. Yazyev, M. Troyer, D. Vanderbilt, B. A. Bernevig, and A. A. Soluyanov, Phys. Rev. B **95**, 075146 (2017).

[25] Q. Wu, S. Zhang, H.-F. Song, M. Troyer, and A. A. Soluyanov, Comput. Phys. Commun. **224**, 405 (2018).

[26] See Supplemental Material at http://link.aps.org/supplemental/10.1103/PhysRevMaterials.2.114204 for details regarding the optimized lattice parameters, electronic band structures, electronic density of states (DOS), phonon spectrum, and atom-projected phonon DOS for all the studied materials. The surface electronic structure, surface phonon spectrum, thermoelectric properties, and results of crystal stability and elastic properties of the predicted TaSb compound are illustrated in the SM [56–71].

[27] B. Q. Lv, H. M. Weng, B. B. Fu, X. P. Wang, H. Miao, J. Ma, P. Richard, X. C. Huang, L. X. Zhao, G. F. Chen, Z. Fang, X. Dai, T. Qian, and H. Ding, Phys. Rev. X **5**, 031013 (2015).

[28] S.-Y. Xu, I. Belopolski, N. Alidoust, M. Neupane, G. Bian, C. Zhang, R. Sankar, G. Chang, Z. Yuan, C.-C. Lee, S.-M. Huang, H. Zheng, J. Ma, D. S. Sanchez, B. Wang, A. Bansil, F. Chou, P. P. Shibayev, H. Lin, S. Jia, and M. Z. Hasan, Science **349**, 613 (2015).

[29] L. Lu, Z. Wang, D. Ye, L. Ran, L. Fu, J. D. Joannopoulos, and M. Soljačić, Science **349**, 622 (2015).

[30] A. A. Soluyanov, D. Gresch, Z. Wang, Q. Wu, M. Troyer, X. Dai, and B. A. Bernevig, Nature **527**, 495 (2015).

[31] X. Wan, A. M. Turner, A. Vishwanath, and S. Y. Savrasov, Phys. Rev. B **83**, 205101 (2011).

[32] N. Marzari and D. Vanderbilt, Phys. Rev. B **56**, 12847 (1997).

[33] I. Souza, N. Marzari, and D. Vanderbilt, Phys. Rev. B **65**, 035109 (2001).

[34] P. E. Nielsen and P. L. Taylor, Phys. Rev. B **10**, 4061 (1974).

[35] G. J. Snyder and E. S. Toberer, Nat. Mater. **7**, 105 (2008).

[36] G. D. Mahan and J. O. Sofo, Proc. Natl. Acad. Sci. U.S.A. **93**, 7436 (1996), http://www.pnas.org/content/93/15/7436.full.pdf.

[37] I. Terasaki, Y. Sasago, and K. Uchinokura, Phys. Rev. B **56**, R12685 (1997).

[38] K. Takahata, Y. Iguchi, D. Tanaka, T. Itoh, and I. Terasaki, Phys. Rev. B **61**, 12551 (2000).

[39] T. Okuda, K. Nakanishi, S. Miyasaka, and Y. Tokura, Phys. Rev. B **63**, 113104 (2001).

[40] B. Peng, H. Zhang, H. Shao, H. Lu, D. W. Zhang, and H. Zhu, Nano Energy **30**, 225 (2016).

[41] M. Markov, X. Hu, H.-C. Liu, N. Liu, S. J. Poon, K. Esfarjani, and M. Zebarjadi, Sci. Rep. **8**, 9876 (2018).

[42] G. Kresse and J. Furthmüller, Phys. Rev. B **54**, 11169 (1996).

[43] G. Kresse and D. Joubert, Phys. Rev. B **59**, 1758 (1999).

[44] J. P. Perdew, K. Burke, and M. Ernzerhof, Phys. Rev. Lett. **77**, 3865 (1996).

[45] A. Togo, F. Oba, and I. Tanaka, Phys. Rev. B **78**, 134106 (2008).

[46] A. A. Mostofi, J. R. Yates, Y.-S. Lee, I. Souza, D. Vanderbilt, and N. Marzari, Comput. Phys. Commun. **178**, 685 (2008).

[47] O. Hellman, I. A. Abrikosov, and S. I. Simak, Phys. Rev. B **84**, 180301 (2011).

[48] O. Hellman, P. Steneteg, I. A. Abrikosov, and S. I. Simak, Phys. Rev. B **87**, 104111 (2013).

[49] A. H. Romero, E. K. U. Gross, M. J. Verstraete, and O. Hellman, Phys. Rev. B **91**, 214310 (2015).

[50] S. Nosé, Mol. Phys. **52**, 255 (1984).

[51] W. G. Hoover, Phys. Rev. A **31**, 1695 (1985).

[52] G. K. H. Madsen and D. J. Singh, Comput. Phys. Commun. **175**, 67 (2006).

[53] T. J. Scheidemantel, C. Ambrosch-Draxl, T. Thonhauser, J. V. Badding, and J. O. Sofo, Phys. Rev. B **68**, 125210 (2003).

[54] D. J. Singh, Phys. Rev. B **81**, 195217 (2010).

[55] T. Thonhauser, T. J. Scheidemantel, J. O. Sofo, J. V. Badding, and G. D. Mahan, Phys. Rev. B **68**, 085201 (2003).

[56] S. Goedecker, J. Chem. Phys. **120**, 9911 (2004).

[57] M. Amsler and S. Goedecker, J. Chem. Phys. **133**, 224104 (2010).

[58] F. Jensen, *Introduction to Computational Chemistry* (John Wiley & Sons, Chichester, England, 2017).

[59] M. Sicher, S. Mohr, and S. Goedecker, J. Chem. Phys. **134**, 044106 (2011).

[60] S. Singh, A. C. Garcia-Castro, I. Valencia-Jaime, F. Muñoz, and A. H. Romero, Phys. Rev. B **94**, 161116 (2016).

[61] S. Singh, W. Ibarra-Hernandez, I. Valencia-Jaime, G. Avendano-Franco, and A. H. Romero, Phys. Chem. Chem. Phys. **18**, 29771 (2016).

[62] O. Pavlic, W. Ibarra-Hernandez, I. Valencia-Jaime, S. Singh, G. Avendaño-Franco, D. Raabe, and A. H. Romero, J. Alloys Compd. **691**, 15 (2017).

[63] J. Murray, J. Taylor, L. Calvert, Y. Wang, E. Gabe, and J. Despault, J. Less-Common Met. **46**, 311 (1976).

[64] S.-Y. Xu, I. Belopolski, D. S. Sanchez, C. Zhang, G. Chang, C. Guo, G. Bian, Z. Yuan, H. Lu, T.-R. Chang, P. P. Shibayev, M. L. Prokopovych, N. Alidoust, H. Zheng, C.-C. Lee, S.-M. Huang, R. Sankar, F. Chou, C.-H. Hsu, H.-T. Jeng, A. Bansil, T. Neupert, V. N. Strocov, H. Lin, S. Jia, and M. Z. Hasan, Sci. Adv. **1**, e1501092 (2015).

[65] T. Besara, D. A. Rhodes, K.-W. Chen, S. Das, Q. R. Zhang, J. Sun, B. Zeng, Y. Xin, L. Balicas, R. E. Baumbach, E. Manousakis, D. J. Singh, and T. Siegrist, Phys. Rev. B **93**, 245152 (2016).

[66] Z. K. Liu, L. X. Yang, Y. Sun, T. Zhang, H. Peng, H. F. Yang, C. Chen, Y. Zhang, Y. F. Guo, D. Prabhakaran, M. Schmidt, Z. Hussain, S. K. Mo, C. Felser, B. Yan, and Y. L. Chen, Nat. Mater. **15**, 27 (2016).

[67] Z.-J. Wu, E.-J. Zhao, H.-p. Xiang, X.-f. Hao, X.-j. Liu, and J. Meng, Phys. Rev. B **76**, 054115 (2007).

[68] S. Singh, I. Valencia-Jaime, O. Pavlic, and A. H. Romero, Phys. Rev. B **97**, 054108 (2018).

[69] M. Born and K. Huang, *Dynamical Theory of Crystal Lattices* (Clarendon Press, Oxford, 1954).

[70] R. Hill, Proc. Phys. Soc. Section A **65**, 349 (1952).

[71] S. Pugh, Philos. Mag. Ser. 7 **45**, 823 (1954).